Hindawi
Structural Control and Health Monitoring
Volume 2023, Article ID 4101604, 18 pages
https://doi.org/10.1155/2023/4101604

Research Article

The Use of Shape Accel Array for Deformation Monitoring and Parameter Inversion of a 300 m Ultrahigh Rockfill Dam

Zhitao Ai[1,2] **Gang Ma**[1,2] **Guike Zhang**[3] **Xiang Cheng**[1,2] **Quancheng Zou**[1,2] **and Wei Zhou**[1,2]

[1]*State Key Laboratory of Water Resources Engineering and Management, Wuhan University, Wuhan 430072, Hubei, China*
[2]*Key Laboratory of Rock Mechanics in Hydraulic Structural Engineering of Ministry of Education, Wuhan University, Wuhan 430072, China*
[3]*YaLong River Hydropower Development Co. Ltd., Chengdu 610051, China*

Correspondence should be addressed to Gang Ma; magang630@whu.edu.cn

Received 21 February 2023; Revised 13 April 2023; Accepted 15 April 2023; Published 27 July 2023

Academic Editor: Francesc Pozo

The global construction of rockfill dams has now surpassed the 300 m height level. Despite great achievements in dam design and construction, monitoring techniques have lagged behind the development of high rockfill dams. Existing deformation monitoring techniques are ill-suited to the high earth and water pressures, and extended monitoring periods are required for ultrahigh rockfill dams. This study introduces, for the first time, the use of a shape accel array (SAA) to monitor internal displacement in a 300 m high earth core rockfill dam. The SAA employs a rope-like array of capacitive MEMS accelerometers for deformation measurement. Compared to conventional monitoring techniques, SAA is a data-intensive monitoring technique. Based on the intensive data obtained from SAA, we employed a parameter inversion method, utilizing multiobjective optimization algorithm, the nondominated sorting genetic algorithm-III (NSGA-III), to inverse the constitutive model parameters of the rockfill dam. The multiobjective parameter inversion method maximizes the use of multisource monitoring data for predicting rockfill dam deformation.

1. Introduction

Rockfill dams, one of the most promising types of dams, have seen remarkable technological advancements in recent years [1]. From 100 to 200 m dams, technology has successfully advanced to building 300 m ultrahigh dams [2]. Since the 1960s, many ultrahigh rockfill dams have been constructed, such as the Chicoasen dam (261 m, Mexico), the Nurek dam (300 m, USSR), the Shuangjiangkou dam (315 m, China), and the Rumei dam (315 m, China). Accurate and long-term monitoring data of these structures contain valuable space-time information that aids in studying the deformation mechanism of rockfill dams, confirming the accuracy of constitutive models, and assessing the safety of design, construction, and operation [3]. Table 1 outlines typical issues of conventional monitoring instruments caused by various factors.

Creating novel monitoring instruments that are appropriate for ultrahigh rockfill dams is crucial due to the difficulties encountered with conventional monitoring instruments, such as sparse monitoring points and massive construction interference. The monitoring instruments should be suitable for the complicated and challenging circumstances of ultrahigh rockfill dams, which involve high pressures and large shears.

Microelectromechanical systems (MEMS) have been applied in various aspects, because they are characterized by their compact size, light weight, and low cost. For example, by integrating gas detecting sensors into MEMS platforms, it is feasible to create miniaturized, portable sensing devices with extremely minimal power requirements [7]. Besides, it is possible to use multiple MEMS inertial measurement units for the robot's position estimation, maintaining real-time updates of its location and operating status, and thus further

Table 1: Conventional instruments and monitoring difficulties.

Instruments	Monitoring difficulties
Horizontal displacement gauge of tensional wire	Steel wire creep, thermal expansion, cold contraction, and the influence of the junction disc on the steel wire support [4]
Hydraulic overflow settlement gauge	The resistance of liquid increases exponentially along a long pipeline and interferes with observations. Better burial technology is needed, such as 1% strictly refined burial gradient, and massive construction interference to provide the connected water-containing pipeline [5]
Electromagnetic settlement gauge	Easily demagnetized during long-term monitoring and large construction impact [6]. During the installation process, a protective tube with a diameter of about one meter is required to protect this instrument. The diameter of the construction impact reaches about three meters

achieving autonomous driving functions [8]. MEMS has made remarkable achievements in the field of biomedicines and has been developed to the extent of manufacturing MEMS microcoils to stimulate biological nerve tissues [9]. High-performance MEMS sensors are in significant demand for geophysical applications, including natural disasters such as earthquake monitoring, earth tides, and volcano activity monitoring, exploration of earthquake, gravity, and magnetic resources, and gravity-assisted navigation, drilling process monitoring [10]. Therefore, it is feasible to apply MEMS to the deformation measurement of rockfill dam engineering.

One of the representatives of deformation measurement using MEMS as the core component is shape accel array (SAA), which achieves precise, continuous, and steady deformation data acquisition. SAA was first studied by Bennett et al. to monitor the deformation of an unstable slope [11] and evaluate the landslide by the monitoring data acquired [12]. Subsequently, Wang et al. successfully applied SAA to seabed landslide monitoring and successfully established a system that could record hydrodynamic data and monitor seabed landslide deformation [13]. Yan et al. used SAA techniques to capture temporal variations in distributed track settlement profiles, analyze track safety issues, and inform track maintenance plans [14]. In our study, we applied SAA to monitor a 300-meter high rockfill dam to reduce the influence of burial on construction and provide more deformation monitoring points. The great information of spatio-temporal information contained support finite element parameter inversion analysis, which works for more accurate prediction of dam deformation.

Sophisticated monitoring instruments and monitoring data are essential for evaluating dam safety and predicting dam deformation accurately. These monitoring data and prediction results can provide a precise assessment of dam safety.

The prediction of dam deformation currently mainly includes data-driven prediction methods based on time series forecasting [15–17], as well as model-driven prediction methods basically based on the finite element method (FEM). FEM plays a crucial role in dam deformation prediction. Many scholars have devoted themselves to studying advanced constitutive models to more accurately characterize the relationship between stress and strain of soil. For example, Guan et al. coupled machine learning with the finite element method to directly learn the constitutive relationship from the data set [18]. In practical FEM calculations, parameters for rockfill dams are often obtained from laboratory experiments or field trials. However, these parameters can be influenced by experimental conditions, scale effects, random sampling, and other factors, which can result in inaccurate parameters that cause great error in FEM calculation [19]. Therefore, it is very important for the FEM calculation of the dam to identify the parameters accurately through appropriate parameter inversion analysis.

Many scholars have studied the parameter inversion analysis method for rockfill dams in recent years. For instance, Yu et al. proposed an effective Bayesian inversion method for reservoir parameters, which utilizes a data-driven error model and considers interactions among predictive performance metrics [20]. Li et al. adopts extreme learning machine (ELM) as a surrogate model to estimate the simulation results of a physical model, utilizing NSGA-II algorithm for multiobjective parameter inversion analysis [21]. Xu and Wu combine an unsaturated seepage model, principal component analysis (PCA), and NSGA-II to obtain more accurate parameters [22]. In addition, many scholars have conducted inverse analysis on various model parameters of concrete dams, including the formulation of objective functions, optimization of surrogate models, selection of multiobjective optimization algorithms, and development of multiobjective decision criteria [23–27]. These innovative works have also inspired the progress of our research. Efficient and accurate parameter inversion methods should be investigated to improve the evaluation of the safety status of rockfill dams. FEM results obtained using parameters acquired through parameter inversion, along with precise monitoring data for dam deformation, may significantly impact the assessment of dam safety.

The main contributions and innovations of this paper are as follows: (1) We use the SAA to acquire crucial information of the deformation of a 300 m rockfill dam. The installation of the SAA in an ultrahigh rockfill dam substantially decreases construction difficulties and the influence of instrument burial, greatly increases monitoring points for dam body deformation, and promotes dam safety monitoring. (2) We utilize the more efficient and dense deformation monitoring data obtained by the SAA. To adapt to the multimaterial zoning and multisource monitoring features at a 300 m rockfill dam, we perform an NSGA-III multiobjective optimization algorithm-based parameter inversion

analysis that uses SAA monitoring data as primary data and additional typical monitoring instrument data as supplementary data.

The overall structure of this paper is as follows: The second section of this paper explains the structure and operating concept of the SAA, while the third section describes its application at the dam. The fourth section details the specific procedure of the parameter inversion method based on NSGA-III. The fifth section applies this approach to multisource settlement monitoring data primarily based on SAAs, then analyzes and summarizes the findings.

2. Structure and Monitoring Principle of the SAA

The SAA uses a high-precision capacitive MEMS accelerometer for continuous acceleration monitoring and employs Kalman filtering to reduce observation system noise. Displacement of each monitoring point is determined by summing the displacements of each SAA part.

2.1. Structure and Monitoring Principle of the SAA. One section of SAA consists of a high-precision capacitive MEMS accelerometer, a rigid pipe, a flexible hose, and cables. The MEMS accelerometer is the most important component and is installed in the middle of the pipe, connected via an RS-485 bus. Data are transferred and stored in an external logger through the cable. The SAA is user-friendly, providing easy access to dam monitoring information through integrated software. Other components make contributions to improving accuracy and simplifying layout. For example, the horizontally embedded SAA is protected by a PE pipe, while the vertically embedded SAA is buried in the inclinometer pipe. The forced centring device is designed to ensure that the SAA can flexibly change position in the center of the inclinometer pipe. Table 2 and Figure 1 show the specific structure and functions of SAA.

2.2. Calculation Method of Monitoring Point Displacement. The MEMS sensors in the SAA are arranged in a linear array. The quaternion or Euler angle approach is used for MEMS accelerometer attitude analysis [28, 29].

The SAA employs only a MEMS accelerometer, making the solution simple. Each section of the SAA measures a point, and the multiple sections of the SAA are linked to monitor multipoints. After solving the data for each section of the SAA, the computed data value at each monitoring point may be acquired. The specific data calculation process is as follows:

2.2.1. Determining Shaft Inclination. The MEMS accelerometer measures acceleration and outputs $(\mathrm{acc}X_i, \mathrm{acc}Y_i, \mathrm{acc}Z_i)$, the acceleration of i th SAA in three different orthogonal directions, (X, Y, Z). In equation (1), the corresponding inclinations can be obtained, where θ_{X_i}, θ_{X_i}, and θ_{X_i} denote the inclination angle formed by the current time position of the SAA and the initial position, respectively, A is the constant value bias of the MEMS accelerometer, K is the calibration factor of the MEMS accelerometer, and G is the gravitational acceleration.

$$\left.\begin{aligned} \mathrm{acc}X_i &= A + K \cdot G \cdot \sin\theta_{X_i} \\ \mathrm{acc}Y_i &= A + K \cdot G \cdot \sin\theta_{Y_i} \\ \mathrm{acc}Z_i &= A + K \cdot G \cdot \sin\theta_{Z_i} \end{aligned}\right\}. \tag{1}$$

2.2.2. Determining the Displacement Based on the Inclination Angle. The displacement of the nth node may be determined by summing the displacement outputs from each section, given that the length of each SAA is L. The inclination angles of each SAA are calculated in the first step. Then, the displacement of the nth monitoring point can be obtained according to the following equation:

$$\left.\begin{aligned} X_n &= L\sum_1^n \sin\theta_{X_i} = L\sum_1^n\left(\frac{\mathrm{acc}X_i - A}{K \cdot G}\right) \\ Y_n &= L\sum_1^n \sin\theta_{Y_i} = L\sum_1^n\left(\frac{\mathrm{acc}Y_i - A}{K \cdot G}\right) \\ Z_n &= L\sum_1^n \sin\theta_{Z_i} = L\sum_1^n\left(\frac{\mathrm{acc}Z_i - A}{K \cdot G}\right) \end{aligned}\right\}. \tag{2}$$

The two-axis MEMS accelerometer is often utilized in place of the three-axis MEMS accelerometer in practical engineering applications due to its lower cost. In terms of computation, SAA using two-axis and tri-axis MEMS accelerometers differs by one additional axis and one fewer axis.

3. Application of the SAA in an Ultrahigh Central Core Rockfill Dam Project

The SAA in this research is manufactured by Beijing Shengkerui Technology Co., Ltd. For settlement monitoring, the SAA employs two-axis MEMS accelerometers, whereas three-axis MEMS accelerometers are used for measuring horizontal displacement.

3.1. Engineering Background of a Central Core Rockfill Dam. The dam in our research, situated on a river in China, is a rockfill core dam with a crest elevation of 2878.00 m, bottom elevation of 2582.00 m, riverbed dam height of 295.00 m, and core wall top width of 6.00 m. It comprises of an impervious body, filter layer, transition layer, and rockfill area. The seepage-proof body has a straight core wall of gravel soil, while the shell is filled with rockfill material. The core wall and dam shell rockfill include filter and transition layers. A 1.0 m thick concrete cover plate is placed on the bank slope between the core wall and dam

Table 2: Components and function table of the SAA.

Components	Function
High-precision MEMS accelerometer	Measure the acceleration of the dam deformation and then accurately obtain the displacement of the monitoring point, the core component of the SAA
Rigid pipe	Protect the MEMS accelerometer, provide strong shear resistance, torsion resistance, and tensile resistance
Flexible hose	Make the SAA installation convenient so that the arrangement is flexible and customizable based on the demands for monitoring and detecting dam deformation
Forced centring device	Ensures that the MEMS accelerometer can deform with the dam deformation, measures the acceleration, and gets the displacement
Orientation and guide wheels	Ensure that the SAA can be easily taken out of the pipeline to prevent it from being stuck when it is installed in the pipeline
Fixed depression device	Prevent large errors of subsequent monitoring points caused by excessive movement of the starting point and facilitate the installation of the SAA by pressing it into the PE hose

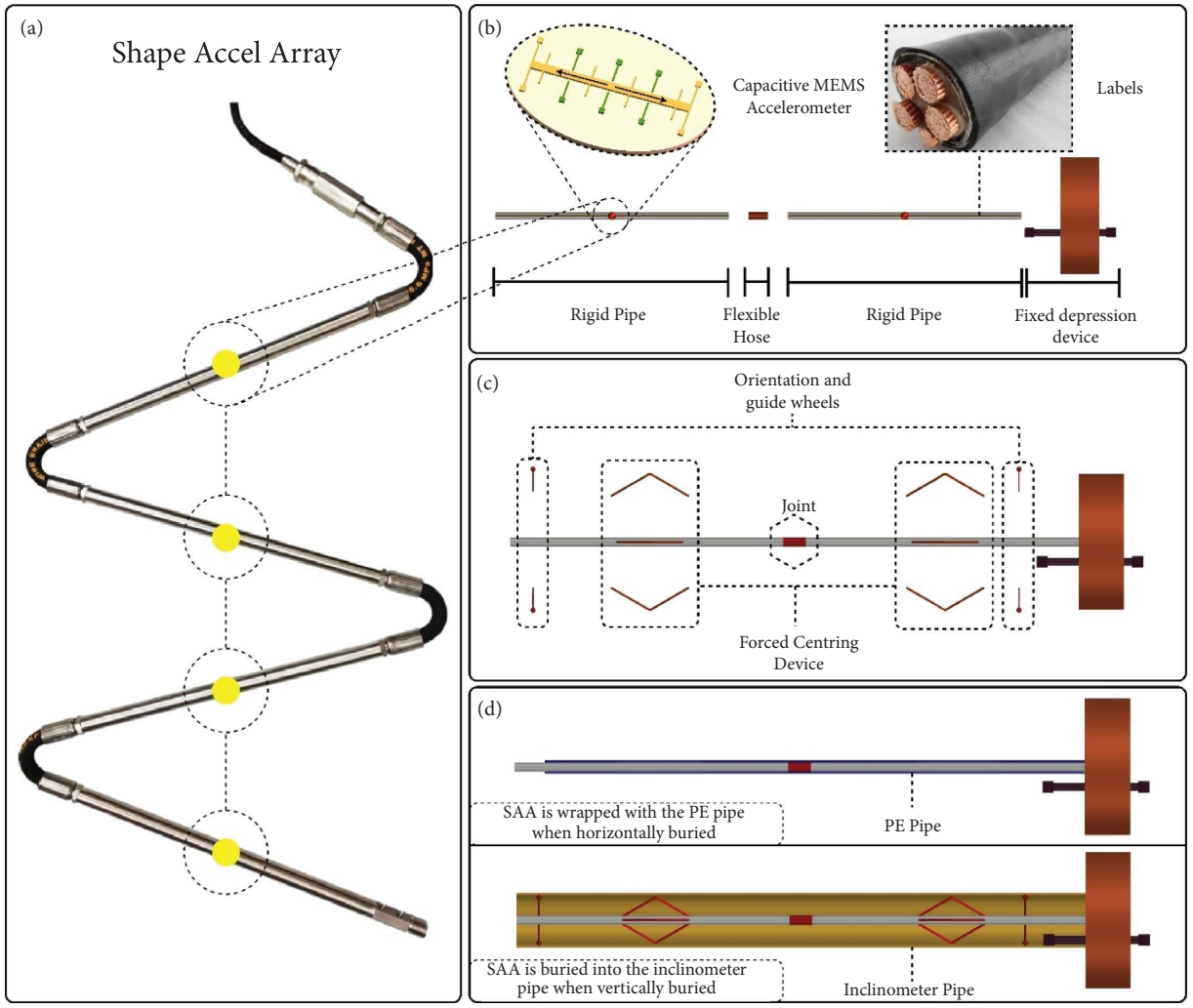

Figure 1: Structure diagram of the SAA. (a) Appearance of SAA. (b) Each part of SAA. (c) Auxiliary device. (d) Monitoring SAA.

abutment on both sides, with a 4.0 m thick contact clay at the core wall-plate interface. Upstream and downstream of the core wall are two layers of filter protection dirt.

The central core rockfill dam is equipped with various innovative monitoring equipment, including the SAA, pipe robots [30], and distributed optical fibre monitoring

instruments [31, 32], in addition to conventional monitoring instruments such as hydraulic overflow settlement gauge, horizontal displacement gauge of tensional wire, electromagnetic settlement gauge, and cross beam settlers. These instruments provide multisource data, which can be fused to create an integrated intelligent safety analysis platform for the dam body. The SAA is the representative innovative internal monitoring device installed in the upstream and downstream rockfill areas and gravel soil core wall of the dam. The project and dam material zoning map is shown in Figure 2.

3.2. Installation Process of the SAA in the Rockfill Dam. The SAA embedding process for this rockfill dam is significantly easier compared to the challenging construction technology required by horizontal displacement gauges of tensional wire and hydraulic overflow settlement gauges. The embedding procedures of SAA are as follows:

To monitor the uneven settling of the dam, SAAs are embedded at different elevations in the upstream rockfill region and the core wall of the rockfill dam, with a simpler installation process than traditional inclinometer tube displacement meters. First, we need to transport the SAA to the construction site and inspect the instruments to ensure they are in good condition. After confirming that the instruments are not damaged during manufacturing or transportation, we apply butter for lubrication on the SAA and place it into the PE pipe. We connect the SAA to the solar power generation device to ensure long-term automated monitoring. However, the hard retaining wall of the SAA is susceptible to brittle fracture, which can lead to failure of the SAA. To prevent such damage, the pipes can be filled with fine sand instead of cement. To embed the SAA in the dam, a trench of x m × 1.5 m × 1.3 m is excavated along the dam axis at the cushion layer location. After leveling the trench bed, a 23 cm thick layer of clay is backfilled and compacted manually. The SAA is then surrounded with a PE pipe, fixed to the cushion, and filled with concrete mortar, surrounding the sensor with 55 cm of fine sand and backfilling with contact clay follows. After manually and uniformly compressing the trench with a vibrator, the dam filling material is used to finish the embedding. Figure 3 illustrates the SAA embedding process.

3.3. Layout of the SAA in the Rockfill Dam. The rockfill dam includes 13 sets of SAAs that are organized in a total length of 1147 meters. The SAA includes a two-axis MEMS accelerometer to reduce expenses. Figure 4 depicts the precise burial position and length of the SAA.

The layout drawings illustrate the horizontal placement of SAA on the core wall section and the 3-3 monitoring section with a 1 m spacing, featuring closely spaced monitoring points. The length of 1147 meters of SAA in the rockfill dam provides extensive monitoring data over an extended period and spatial range, surpassing the limitations of hydraulic overflow settlement gauges and electromagnetic settlement gauges with wider measurement intervals and vertical arrangement, respectively.

3.4. Analysis of SAA Data in the Rockfill Dam. The IN-R11 and IN-R12 SAAs were installed vertically within the rockfill dam to measure horizontal displacement. IN-R12 was intended to be buried after filling the top of the dam, but its installation was delayed due to material shortages and a limited monitoring period. The other SAAs were installed horizontally to measure settlement. The position of each instrument's monitoring point is calculated based on the origin at the contact point between the instrument and the dam body. Monitoring data of IN-R1 to IN-R7, and IN-R11 are presented in Figure 5.

Based on the data collected from different SAAs, overall monitoring data conform to the deformation law of a rockfill dam. The monitoring data from SAAs showed the following patterns: the settlement in the middle of the core wall is greater than that near the riverbank; there is not much difference in the settlement quantity between both sides of the dam with the central axis as the reference, which confirms the rationality of the SAA monitoring data; over time, the settlement amount of the dam body shows an increasing trend. As for horizontal displacement, only the IN-R11 data are available as a reference. Overall, the downstream displacement measured by SAA increases over time and the pattern presented spatially, due to the influence of water storage, has certain reference value.

Certain embedded SAAs are damaged, with certain monitoring points exhibiting erratic variations. Earlier research indicates that the load distribution within rockfill dams is nonuniform, similar to that of the loads of train tracks, leading to rheological soil deformation. This may cause inconsistent pressure on embedded SAAs and continuing plastic deformation of the soil mass, potentially changing the observation data's point or damaging the instrument [14, 32].

4. Multiobjective Parameter Inversion Method Based on Multisource Monitoring Data

Parameter inversion is a common approach to determine rockfill dam calculation parameters. Multiobjective parameter inversion is employed, utilizing deformation monitoring data from various instruments, multimaterial zoning, and the objective function value based on the degree of fitting between deformation monitoring and calculation values. A constitutive model, parameters, multiobjective functions, optimization algorithm, and machine learning surrogate model are required for this approach.

4.1. Constitutive Model Selection. Stress and deformation calculations of ultrahigh rockfill dam and parameter inversion both require a suitable rockfill constitutive model.

Zhang et al. [33] compared the rockfill constitutive model under the complex stress path of the rockfill dam and concluded that Duncan-Chang EB, one of the most well-known nonlinear elastic models, can describe the nonlinear relation of rock deformation more accurately. The parameters of the Duncan-Chang EB model have simple measurements and clear physical concepts. This model is widely applied in the design of rockfill dams and has many engineering reference bases [34]. As a result, the constitutive model for the FEM computation of this ultrahigh rockfill dam is the Duncan-Chang EB model.

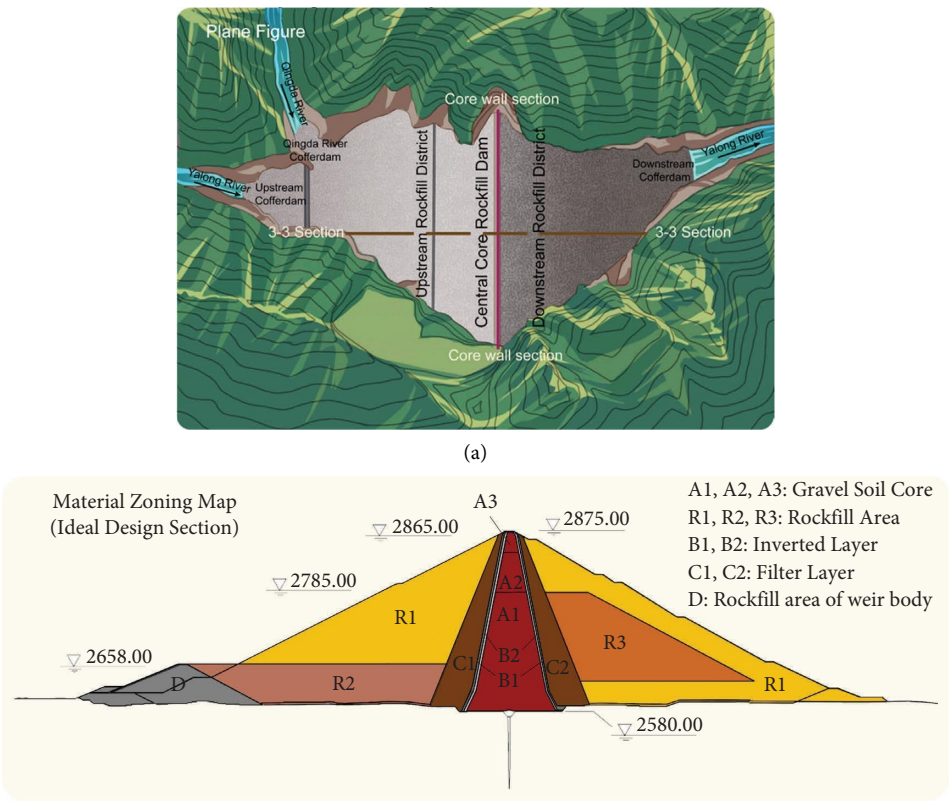

Figure 2: Layout plan and dam material zoning map of the ultrahigh rockfill dam project. (a) The specific horizontal plane layout. (b) Dam material zoning map.

Figure 3: Photographs of embedding the SAA at the construction site. (a) Transport the packaged SAA to the construction site. (b) On-site SAA inspection. (c) Apply butter to the SAA and place it in the PE pipe. (d) Burying the SAA in the trench. (e) Solar power generation system. (f) Connection between generation system and SAA.

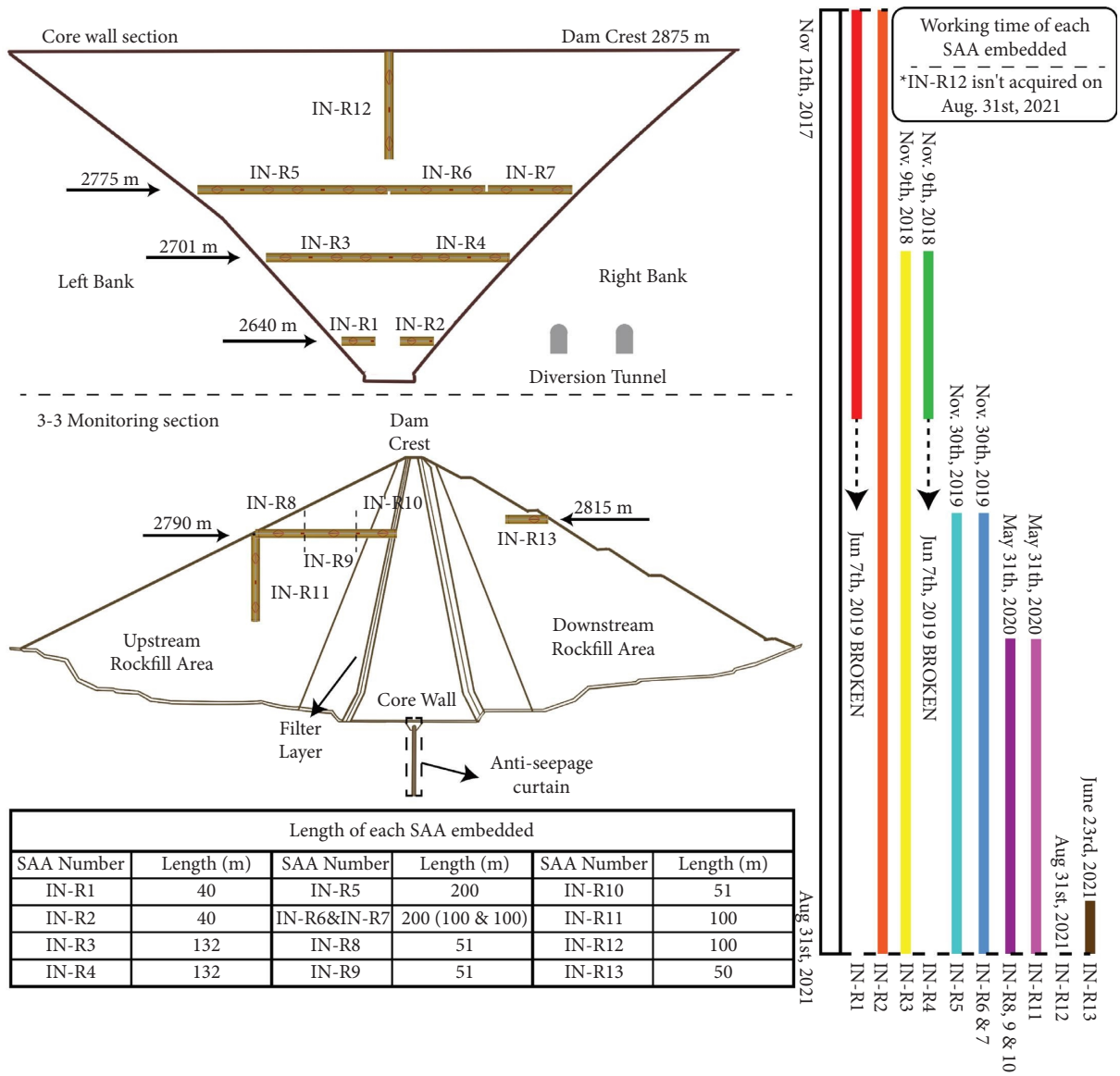

Length of each SAA embedded					
SAA Number	Length (m)	SAA Number	Length (m)	SAA Number	Length (m)
IN-R1	40	IN-R5	200	IN-R10	51
IN-R2	40	IN-R6&IN-R7	200 (100 & 100)	IN-R11	100
IN-R3	132	IN-R8	51	IN-R12	100
IN-R4	132	IN-R9	51	IN-R13	50

Figure 4: Space-time distribution diagram of the SAA layout.

The tangent elastic modulus, unloading elastic modulus, and tangent bulk modulus of the Duncan-Chang EB model are calculated as follows:

$$E_t = KP_a\left(\frac{\sigma_3}{P_a}\right)^n\left[1 - R_f\frac{(\sigma_1 - \sigma_3)(1 - \sin\varphi)}{2c\cos\varphi + 2\sigma_3\sin\varphi}\right], \quad (3)$$

$$E_{\text{ur}} = K_{\text{ur}}P_a\left(\frac{\sigma_3}{P_a}\right)^{n_{\text{ur}}}, \quad (4)$$

$$B_t = K_bP_a\left(\frac{\sigma_3}{P_a}\right)^m, \quad (5)$$

where E_t is the tangent elastic modulus; K is the tangent modulus; n is the tangent modulus index; E_{ur} is the unloading rebound elastic modulus; K_{ur} is the unloading modulus; n_{ur} is the unloading modulus index; B_t is the tangent bulk modulus; K_b is the bulk modulus; m is the bulk modulus index and R_f is the material failure ratio; c is the cohesion of the material; P_a is the unit atmospheric pressure; and φ is the internal friction angle, considering the change with the confining pressure, which is shown as follows

$$\varphi = \varphi_0 - \Delta\varphi\lg\left(\frac{\sigma_3}{P_a}\right), \quad (6)$$

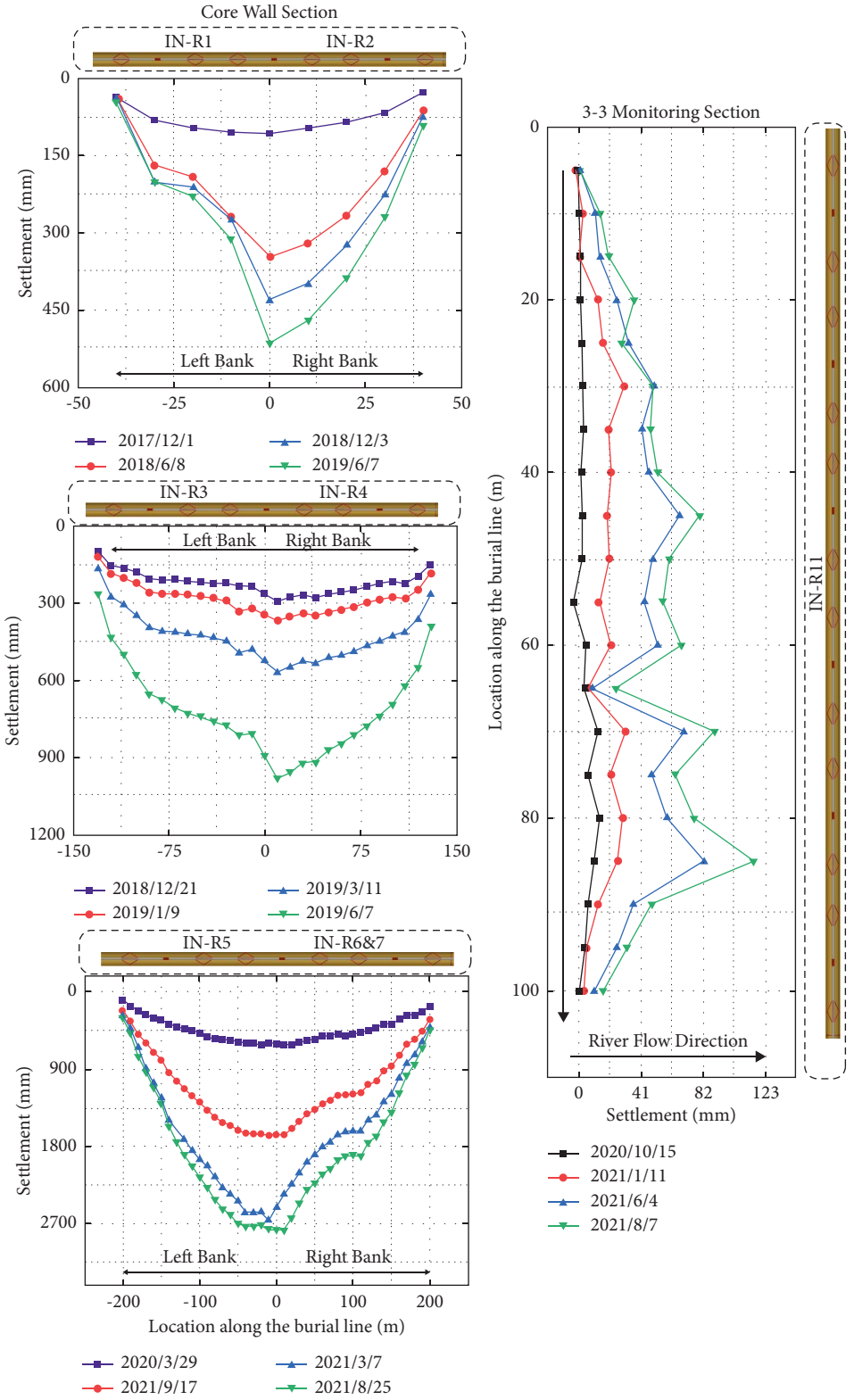

Figure 5: The monitoring data of IN-R1 to IN-R7, and IN-R11.

Algorithm Generation t of the NSGA-III procedure

Input H structured reference points Z^s or supplied aspiration points Z^a, parent population P_t

Output P_{t+1}

1. $S_t = \emptyset, i = 1$
2. $Q_t = \text{Recombination} + \text{Mutation}(P_t)$
3. $R_t = P_t \cup Q_t$
4. $(F_1, F_2, \ldots) = \text{Non-dominated-sort}(R_t)$
5. **Repeat**
6. $S_t = S_t \cup F_i$ and $i = i + 1$
7. **until** $|S_t| \geq N$
8. The last front to be included: $F_j = F_i$
9. **if** $|S_t| = N$ **then**
10. $P_{t+1} = S_t$, break
11. **else**
12. $P_{t+1} = \cup_{j=1}^{j-1} F_j$
13. Points to be chosen from $F_j : K = N - |P_{t+1}|$
14. Normalize objectives and create a reference set Z_r: $Normalize(f^n, S_t, Z^r, Z^s, Z^a)$
15. Associate each member with a reference point: $[\pi(s), d(s)] = Associate(S_t, Zr)$ % $\pi(s)$: closest reference point, d: distance between s and $\pi(s)$
16. Compute niche count of reference point $j \in Z^r : \rho_j = \sum_{s \in S_t / F_j} ((\pi(s) = j)?1:0)$
17. Choose K members once a time from F_j to construct $P_{t+1} : Niching(K, \rho_j, \pi, d, Z_r, F_j, P_{t+1})$
18. **end if**

Figure 6: Procedure of NSGA-III.

where φ_0 is the value of φ when σ_3 is equal to the unit atmospheric pressure and $\Delta\varphi$ is the coefficient of change of the friction angle. The Duncan–Chang E-B model includes 9 main parameters, K, n, K_b, m, R_f, c, φ, K_{ur} and n_{ur}.

A Merchant viscoelastic model based on exponential attenuation is also used to account for the rheological deformation of rockfill dams over time. Equations (7) to (9) can be used to express the rheological deformation, final volumetric rheology, and final shear rheology of a rockfill dam as follows:

$$\varepsilon_t = \varepsilon_f\left(1 - e^{-\lambda t}\right), \tag{7}$$

$$\varepsilon_{\text{Vf}} = \alpha\left(\frac{\sigma_3}{P_a}\right)^{n_1} + \beta\left(\frac{q}{P_a}\right)^{n_2}, \tag{8}$$

$$\gamma_f = \delta\left(\frac{S_l}{1 - S_l}\right)^{n_3}, \tag{9}$$

where ε_t is the rheological deformation; ε_f is the final flow variable over time; ε_{Vf} is the final volume flow variable; γ_f is the final shear rheology; and λ, α, β, δ, n_1, n_2, and n_3 are the seven calculation parameters of the rheological model, where λ reflects the rheological rate and α, β and δ reflect the final rheological deformation.

4.2. Multiobjective Function. Parameter inversion involves finding appropriate parameters to approximate the monitored displacement value and calculated displacement value. Relevant objective functions in different material zones of high rockfill dams are constructed, and deformation monitoring data from several monitoring sensors are introduced. Equation (10) shows the constructed multiobjective function as follows:

$$F(x) = \begin{cases} f^{(1)}\left[\left(x_i^{(1)}, x_i^{(1)*}\right)\Big|_{i=1,2,\cdots,m^{(1)}}\right], \\ f^{(2)}\left[\left(x_i^{(2)}, x_i^{(2)*}\right)\Big|_{i=1,2,\cdots,m^{(2)}}\right], \\ \cdots \\ f^{(n)}\left[\left(x_i^{(n)}, x_i^{(n)*}\right)\Big|_{i=1,2,\cdots,m^{(n)}}\right], \end{cases} \tag{10}$$

where the function $f(x)$ contains n optimization objective functions, and x_i and x_i^* are the monitoring displacement value and FEM calculation value of $m^{(n)}$ internal monitoring points selected from the nth material partition of the dam body.

4.3. Multiobjective Optimization Algorithm. The objective optimization method has been effectively used in various areas of research; it originated from multiobjective optimization algorithms with exceptional performance, such as NSGA [35–37], PSO [38, 39], and Jaya [40, 41]. Among many multiobjective optimization algorithms, NSGA can ensure the uniform distribution of the nondominated optimal solution, the diversity of the population, and high computational efficiency [42–44].

Deb and Jain [45] and Jain and Deb [46] updated the NSGA algorithm to NSGA-III in 2018. The core foundation of the NSGA-III algorithm is GA. A rapid nondominated sorting algorithm, present and associated reference points, and other selection mechanisms are used to improve population individuals, iterate to the convergence algebra, and search for a Pareto optimal solution set in genetic operator selection. Using NSGA-III, we solve parameter inversion as a multiobjective optimization problem. Figure 6 depicts the generational flow of NSGA-III.

4.4. Machine Learning Surrogate Model. Calculating objective function values for all parameter combination individuals for each target space through FEM demands significant computing space and time. The machine learning regression algorithm's superior simulation capacity can replace FEM calculation in the iterative process and increase the efficiency of parameter inversion calculation by mapping material parameters to deformation calculation results.

We train samples using Support Vector Machine (SVM), Random Forest (RF), Extreme Gradient Boost (XGBoost), and Artificial Neural Network (ANN). Besides, we use the mean absolute error ratio (MAPE), root mean square error (RMSE), and the determination coefficient (R^2) to evaluate each machine learning surrogate model and choose the best one. MAPE, RMSE, and R^2 are calculated as follows:

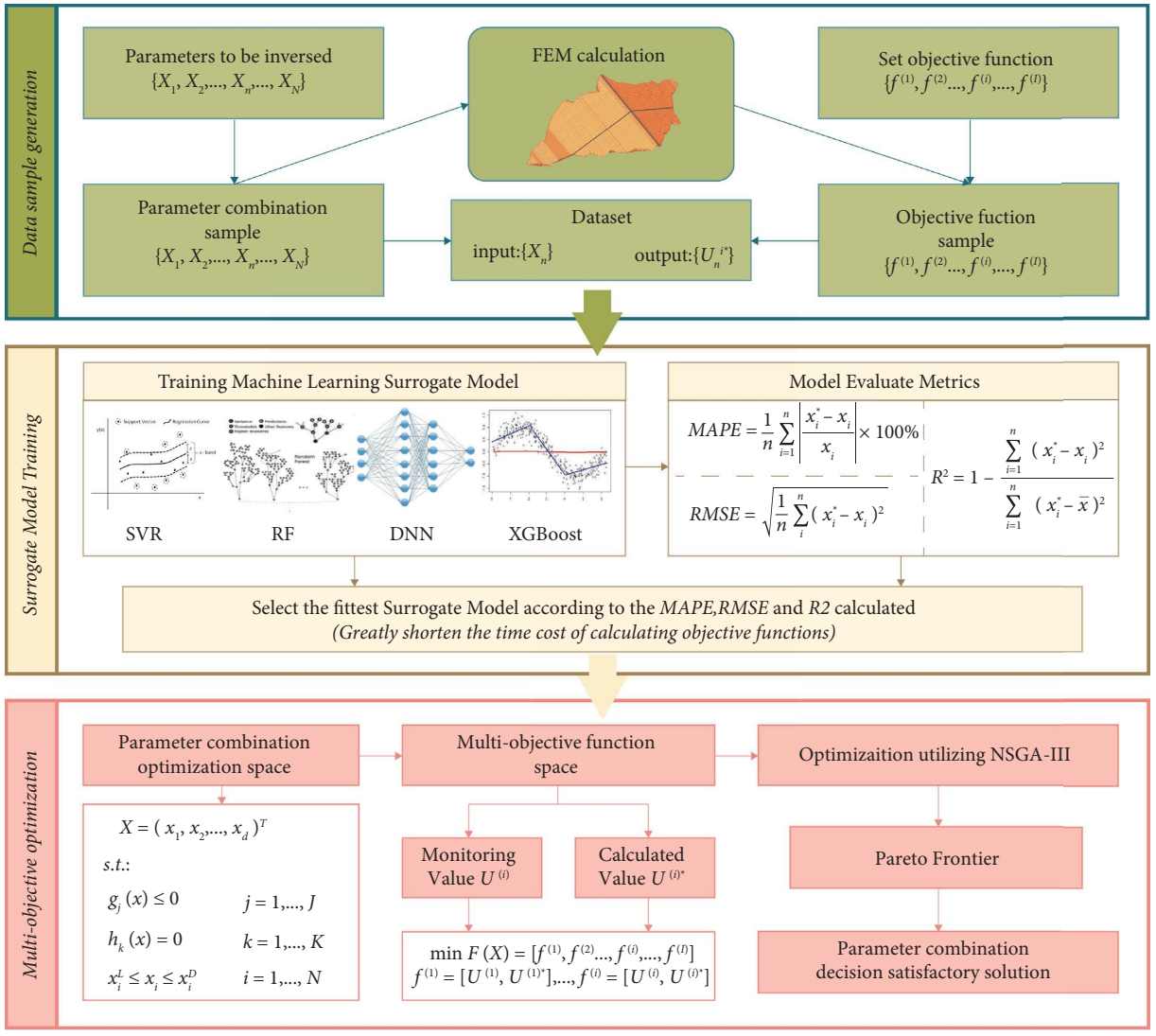

Figure 7: Multiobjective parameter inversion process of rockfill dam.

$$\text{MAPE} = \frac{1}{n}\sum_{i=1}^{n}\left|\frac{x_i^* - x_i}{x_i}\right| \times 100\%, \tag{11}$$

$$\text{RMSE} = \sqrt{\frac{1}{n}\sum_{i}^{n}(x_i^* - x_i)^2}, \tag{12}$$

$$R^2 = 1 - \frac{\sum_{i=1}^{n}(x_i^* - x_i)^2}{\sum_{i=1}^{n}(x_i^* - \bar{x})^2}, \tag{13}$$

where x_i^* is the prediction results of the centralized surrogate model and x_i is the actual result.

4.5. Multiobjective Parameter Inversion Process. Based on the multiobjective function construction strategy described above, the NSGA-III multiobjective optimization algorithm and machine learning surrogate model are used to propose a multiobjective parameter inversion method that can adapt to the multimaterial zoning characteristics of ultrahigh rockfill dams and fully utilize multisource deformation monitoring data. Figure 7 shows the parameter inversion method.

5. Application of Inversion Based on SAA and Other Multisource Monitoring Data

It is worth mentioning that the FEM calculations in this paper were performed using the model that we developed based on ABAQUS. The surrogate model and multiobjective optimization algorithm were implemented using Python and can be found in the open-source libraries Keras and Pymoo, respectively.

5.1. Establishment of a Multiobjective Function Model and Parameter Selection. Because there are many multisource deformation monitoring points of the ultrahigh rockfill dam

Table 3: Number of inversion monitoring points selected in each material partition and monitoring instrument.

	SAA	Hydraulic overflow settlement gauges	Electromagnetic settlement gauge	Sum
Core wall	21	0	9	30
Rockfill area I	9	4	3	18
Rockfill area II	0	0	6	6
Rockfill area III	0	12	0	12
Sum	30	16	18	66

and SAA data are densely distributed in time and space, mainly SAA data are chosen when selecting the inversion monitoring points to ensure that instrument performance does not affect calculation accuracy. Inversion computation uses monitoring data from the core wall section and 3-3 section before the first impoundment (December 2020), the second impoundment (June 2021), and the last monitoring period (September 2021). Table 3 shows the selected instrument zones and measuring locations.

Based on the multiobjective function construction method, the 2-norm of the difference between the monitoring settlement value and the calculated settlement value of the selected monitoring points in the four main material partitions of the rockfill area and the core wall area is used as the partition objective function to build a 4-objective optimization model, as shown in the following equation:

$$F(x) = \begin{cases} \min F(x) = \left(f^{(1)}, f^{(2)}, f^{(3)}, f^{(4)}\right)^T, \\ y = \left(y^{(1)}, y^{(2)}, y^{(3)}, y^{(4)}\right)^T, \\ f^{(i)}\Big|_{i=1,2,3,4} = \left[\dfrac{1}{m^{(i)}n^{(i)}} \displaystyle\sum_{j=1}^{m^{(i)}} \sum_{k=1}^{n^{(i)}} \left(\dfrac{U_{jk}^{(i)*}}{U_{jk}^{(i)}} - 1\right)^2\right]^{0.5}, \\ y^{(i)}\Big|_{i=1,2,3,4} = \left\{y_1^{(i)}, y_2^{(i)}, \ldots y_d^{(i)}, \ldots, y_D^{(i)}\right\}, \\ y_d^{(i)\min} \le y_d^{(i)} \le y_d^{(i)\max}, \end{cases} \tag{14}$$

where $f^{(1)}$, $f^{(2)}$, $f^{(3)}$, and $f^{(4)}$ are the objective functions of rockfill areas I, II, and III and the core wall, respectively; $m^{(i)}$ is the number of monitoring points selected in the ith partition; $n^{(i)}$ is the characteristic time point selected for each monitoring point; $U_{jk}^{(i)^*}$ is the settlement calculation value of the jth monitoring point in the zone at the kth time point; and $U_{jk}^{(i)}$ is the corresponding measured value. $y^{(i)}$ is the parameter to be back analysed in the partition, which is K, n, K_b, and m in the Duncan-Chang E-B model and λ, α, β, and δ in the Merchant seven parameter model; $y_d^{(i)\min}$ and $y_d^{(i)\max}$ are the upper and lower limits of the parameters to be back analysed.

5.2. Sample Design and Surrogate Model Training. Considering that it is difficult to ensure the accuracy of the inversion results in the target search space with too many dimensions, some parameters have little impact on the stress and deformation of the dam body, and it is difficult for some parameters to be accurately determined through indoor and on-site experiments. Thus, eight parameters, K, n, K_b, m, λ, α, β, and δ of the Duncan-Chang EB model and Merchant viscoelastic model are finally selected as the parameter set to be back analysed.

The finite element model illustrated in Figure 8 has 150,776 elements and 150,397 nodes. We obtained 520 sets of parameter samples using orthogonal test design and random sample design methods and performed 520 groups of FEM forward computations. These works were carried out using our self-developed secondary development model based on ABAQUS.

We utilize ANN, XGBoost, RF, and SVR for regression. The parameter combinations are used as input and the FEM results are used as output. 75% of the data is used as the training set, while the remaining 25% is used as the testing set. Normalizing the final projected and measured values yields Figure 9. The accuracy and generalization capabilities of the characterization training model increase when RMSE, MAE, and R^2 approach 100%.

Figure 9 shows that the expected output from the ANN training model matches the predicted output best, and each partition has the maximum accuracy. The fitting results of XGBoost and RF are inferior to those of ANN but comparable to SVR. When the sample size and kernel function mapping dimension are enormous, the calculation amount is large, and the fitting effect is low, making the SVR unsuitable. It should be noted that the type of ANN used in this study is the basic fully connected neural network. Based on various metrics shown in Figure 9, ANN is fully capable of fitting parameters to FEM results and outperforms the other three models in this regard.

5.3. Multiobjective Optimization. We utilize NSGA-III to optimize the 4-objective model iteratively. The algorithm's parameters are as follows: the initial population size is 520, the maximum evolutionary algebra is 400, the probability of variation is 0.1, and the cross-over and variation parameters are 30 and 20, respectively. Figure 10 shows the objective function values and mean values for each iteration.

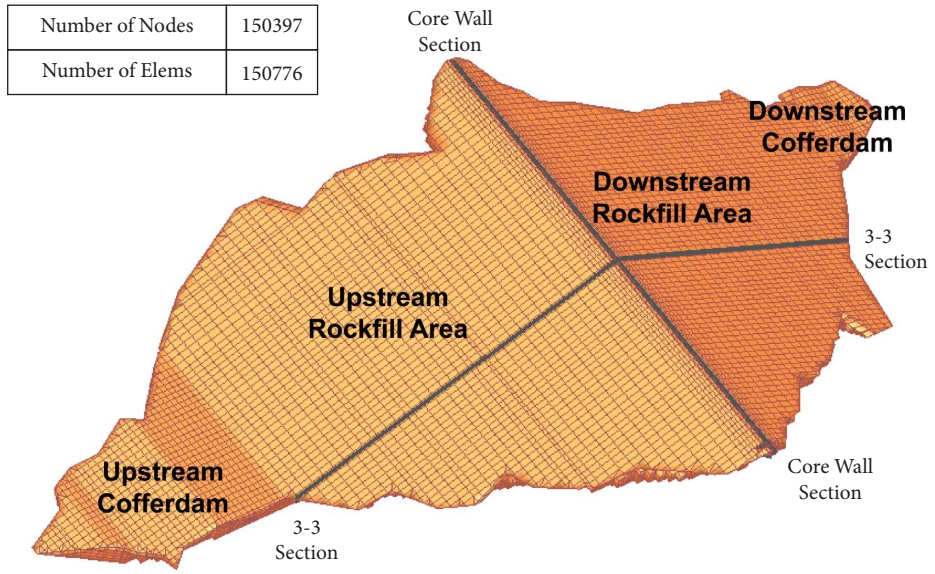

Figure 8: Finite element model of the ultrahigh rockfill dam.

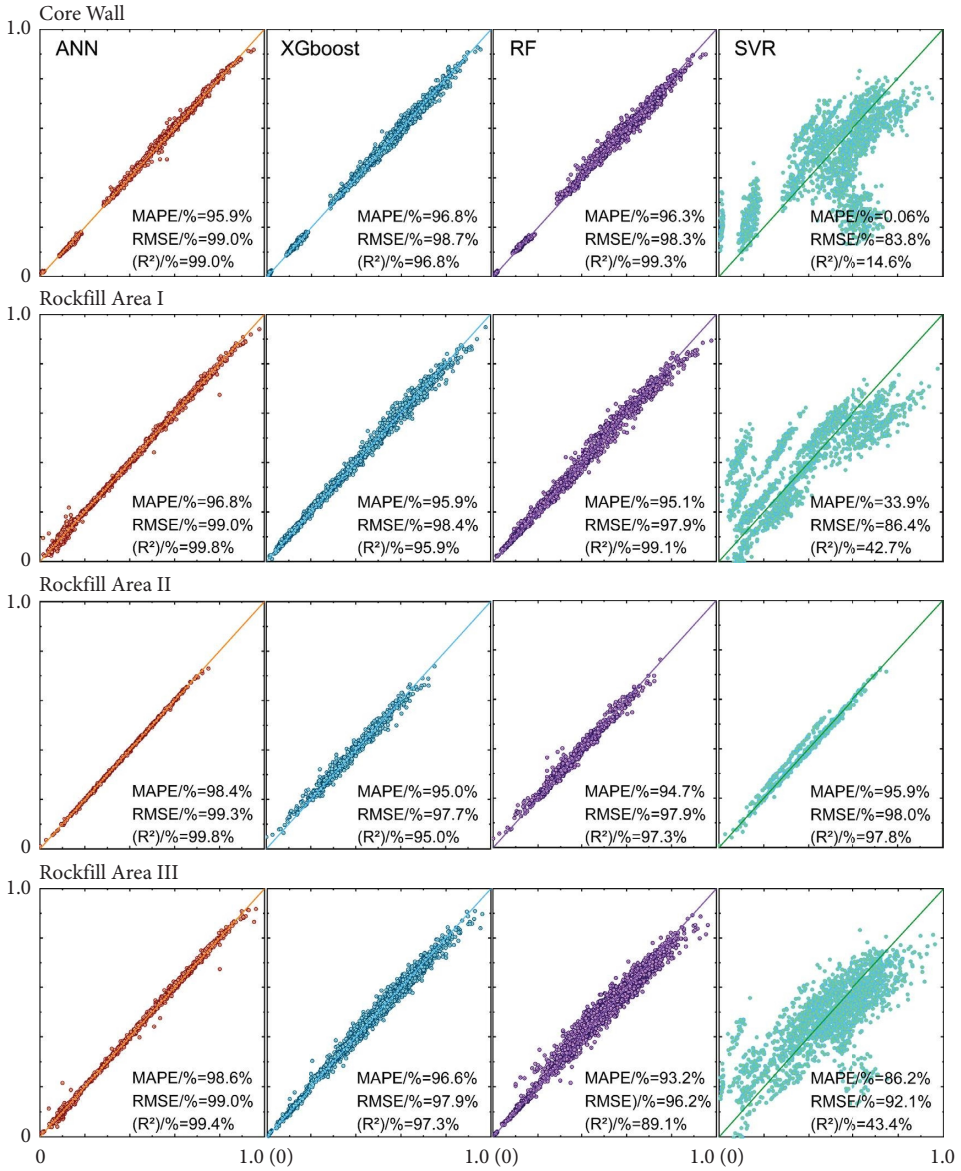

Figure 9: Comparison of the accuracy of different surrogate models. The horizontal and vertical axes are the normalized monitoring values and the predicted values of the proxy model, respectively.

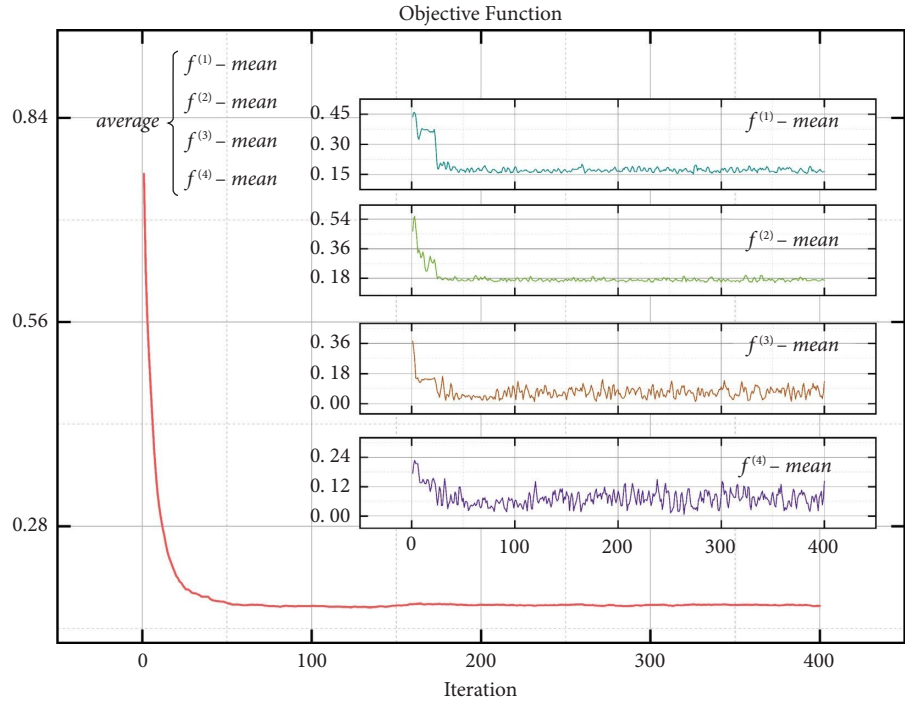

Figure 10: Diagram of the value of the objective function of each material partition.

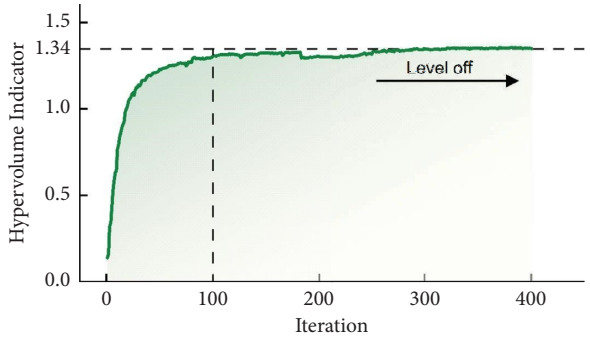

Figure 11: Hypervolume indicator.

The multiobjective evaluation index evaluates the convergence and dispersion of the optimal solution set. The hypervolume indicator is consistent with the optimization solution set. Its physical meaning is the hypercube volume formed by the solution set individual and the reference point in the target space. The larger the indicator value is, the more dominant the optimization solution set. The reference point can be set as (1.1, 1.1, 1.1, 1.1) when the leading edge is unknown. Figure 11 shows the calculated hypervolume indicator.

After 100 generations of NSGA-III iteration, objective function value and the hypervolume indicator show that population evolution converges to a higher level. Figure 12 shows a Pareto frontier with 255 Pareto optimal options after optimization. The linear weights for the goal functions are 0.25 for rockfill area I, 0.20 for rockfill II, 0.25 for rockfill area III, and 0.30 for the core wall. The parameter combination with the minimal value of $0.25f_1 + 0.2f_2 + 0.25f_3 + 0.3f_4$ is the final multiobjective optimization parameter, which is shown as the yellow line in Figure 12.

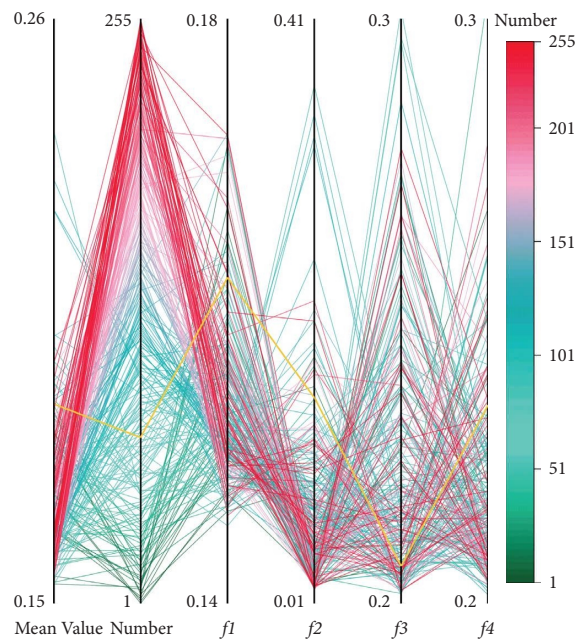

Figure 12: Pareto frontier calculated.

5.4. Evaluation of the Multiobjective Parameter Inversion Effect. To demonstrate the significance of SAA monitoring data in parameter inversion and to validate the rationality of the parameter inversion method proposed, we similarly substitute the parameter inversion results without SAA data

Table 4: Parameter inversion result table.

		Whether SAA data is included (yes/no)	Inversion results			
			Rockfill area I	Rockfill area II	Rockfill area III	Core wall
Duncan–Chang E-B model	K	Y	1840.0	1695.8	1560.5	452.2
		N	1750.2	1653.4	1564.3	270.6
	n	Y	0.427	0.126	0.405	0.611
		N	0.427	0.129	0.404	0.206
	K_b	Y	429.5	557.2	574.0	700.6
		N	153.7	331.7	548.2	697.4
	m	Y	0.29	0.08	0.285	0.582
		N	0.298	0.225	0.277	0.514
Merchant model	λ	Y	3.72×10^{-4}	3.69×10^{-4}	3.64×10^{-4}	3.60×10^{-4}
		N	3.65×10^{-4}	3.77×10^{-4}	3.61×10^{-4}	5.1×10^{-4}
	α	Y	9.83×10^{-3}	9.77×10^{-3}	9.71×10^{-3}	9.72×10^{-3}
		N	1.04×10^{-2}	1.16×10^{-2}	1.04×10^{-2}	2.90×10^{-2}
	β	Y	2.81×10^{-3}	2.80×10^{-3}	2.78×10^{-3}	2.78×10^{-3}
		N	2.98×10^{-3}	3.32×10^{-3}	2.97×10^{-3}	8.31×10^{-3}
	δ	Y	1.50×10^{-2}	1.49×10^{-2}	1.48×10^{-2}	1.48×10^{-2}
		N	1.59×10^{-2}	1.77×10^{-2}	1.58×10^{-2}	4.42×10^{-2}

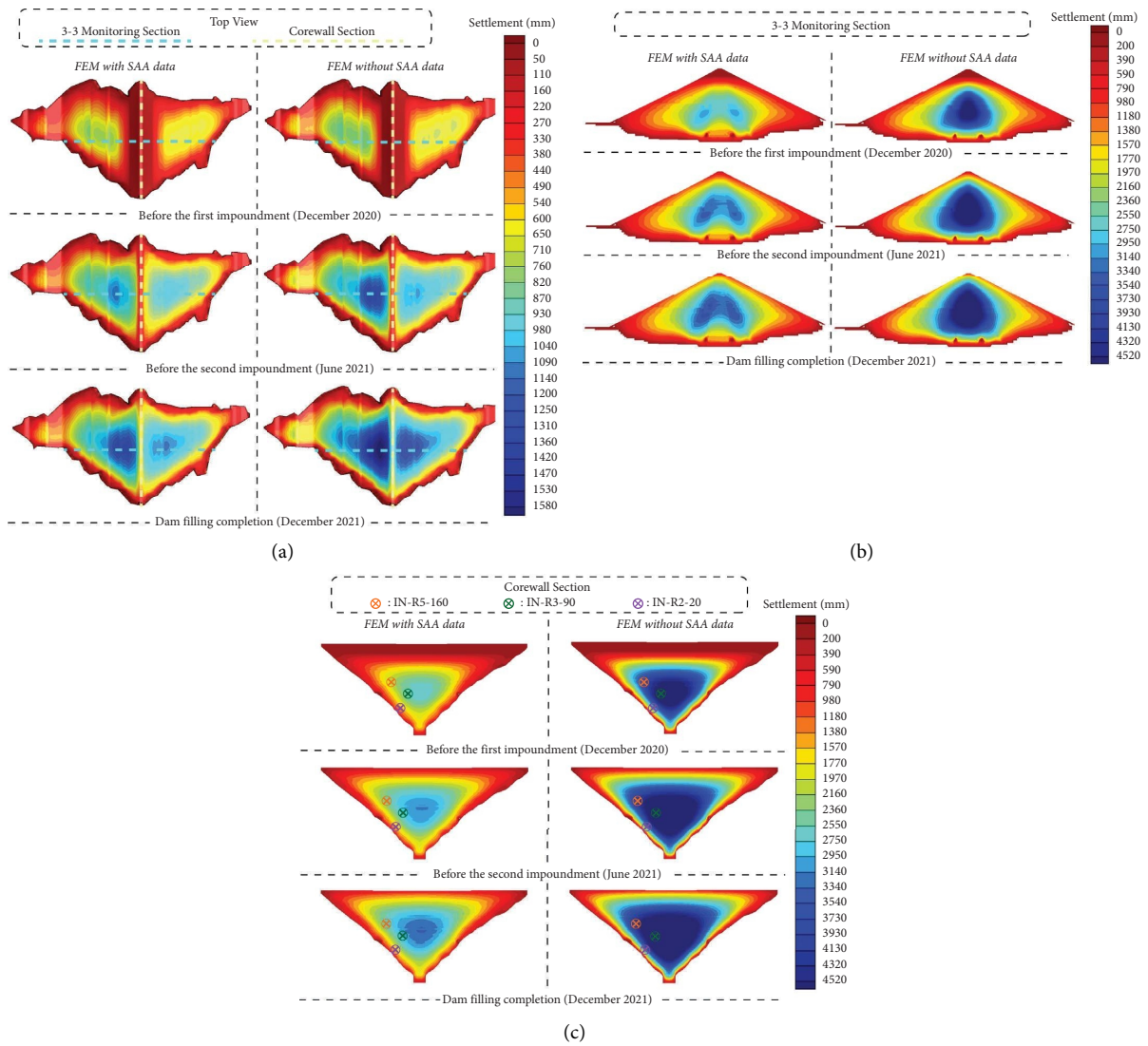

Figure 13: Cloud charts of settlement distribution. (a) Top view of the overall settlement of the dam body. (b) 3-3 monitoring section. (c) Core wall section.

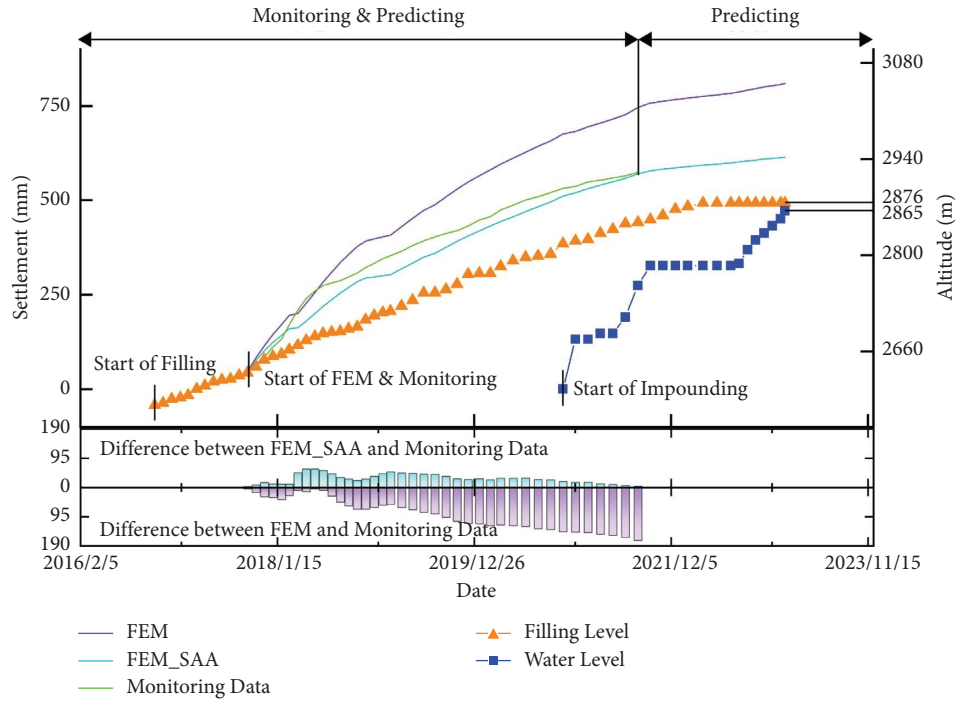

(a)

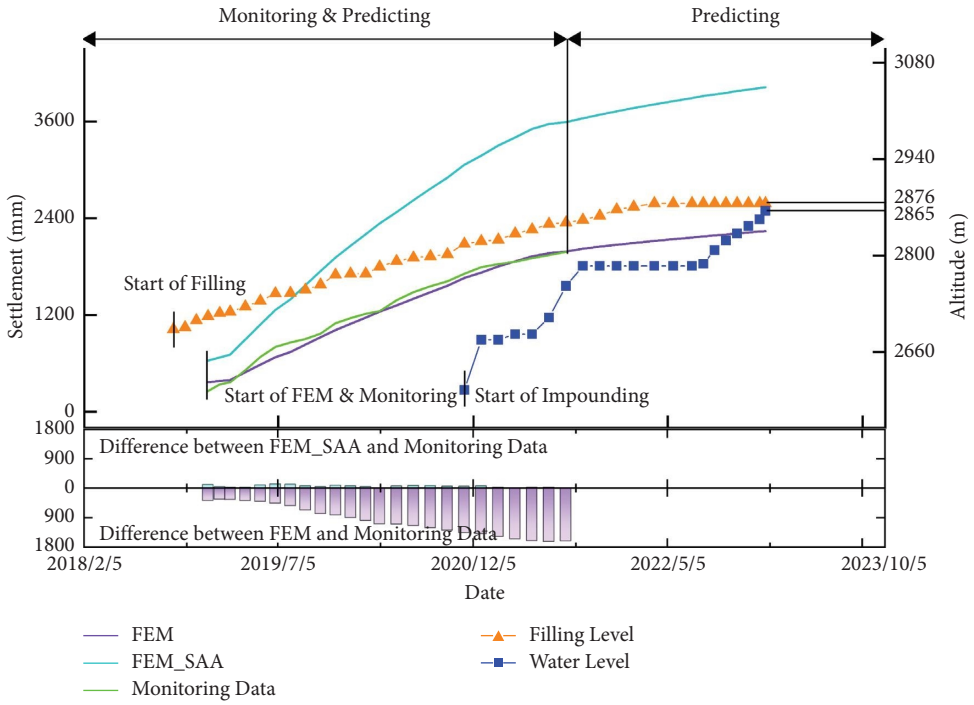

(b)

Figure 14: Continued.

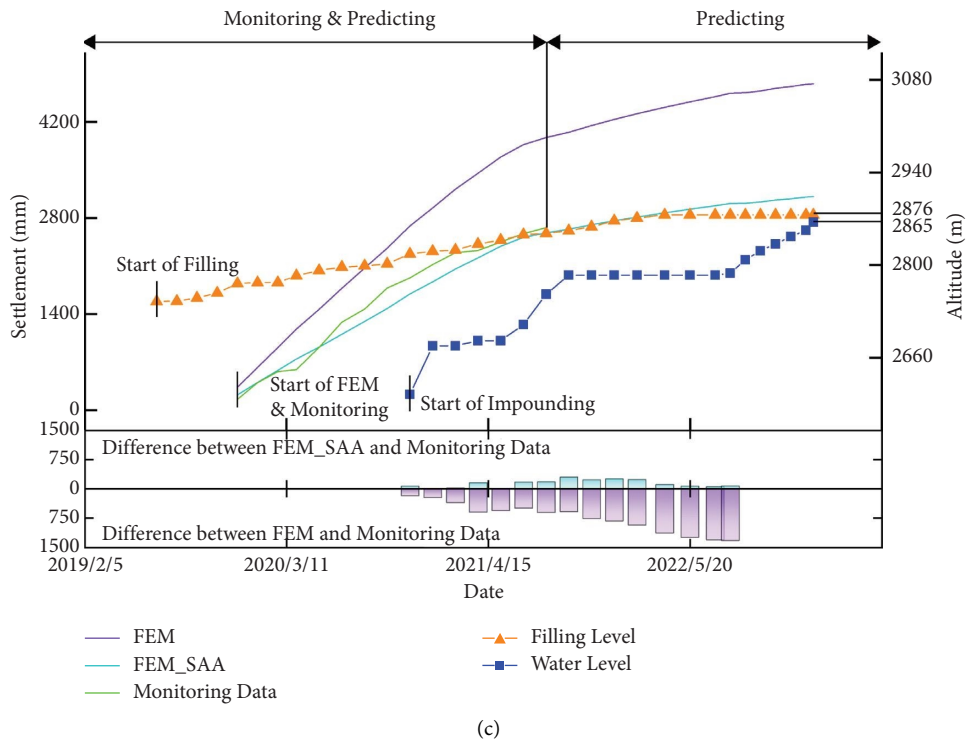

(c)

Figure 14: Comparison of settlement monitoring results and predicted values at some monitoring points. (a) Monitoring point at 20 m for IN-R2. (b) Monitoring point at 90 m for IN-R3. (c) Monitoring point at 160 m for IN-R5.

into the FEM calculation and obtain the results. Table 4 shows inversion values of the parameters.

Table 4 shows that the inclusion of SAA monitoring data has a significant impact on the parameter inversion results, which confirms the importance of SAA in the analysis of parameter inversion. To further verify the effectiveness of the parameters obtained by the inversion method in evaluating the overall safety level of the dam with FEM calculations, we conducted calculations using these two sets of parameters in the finite element model. The result of settlement cloud map of the dam is shown in Figure 13, which displays the top view, the 3-3 monitoring section, and the core wall section.

Based on the calculation results, it can be observed that the inclusion of SAA data in the parameter inversion analysis resulted in lower maximum settlement calculated values during the various stages of dam construction. Prior to the first impoundment in December 2020, the maximum settlement calculated with SAA data was 3.03 m, which accounted for 1.03% of the maximum dam height. Similarly, during the second impoundment in June 2021, the maximum settlement with SAA data was 3.49 m, accounting for 1.18% of the maximum dam height. Finally, at the completion of dam filling in December 2021, the maximum settlement calculated with SAA data was 3.69 m, accounting for 1.25% of the maximum dam height. In contrast, the maximum settlement values calculated without SAA data were higher for all stages of construction, with values of 5.27 m, 5.93 m, and 6.20 m, accounting for 1.79%, 2.01%, and 2.10% of the maximum dam height, respectively. Based on the parameters, the overall FEM result with SAA data of the dam is within a reasonable range, and the distributions and development trends of the FEM results follow the standard rockfill dam deformation laws.

We have extracted the calculated values of some single monitoring points, whose location can be found in the subgraph c in Figure 13, from the FEM calculation with or without SAA data, as well as the instrument monitoring values for comparison. Specific data is illustrated in Figure 14.

Figure 14 indicates that the FEM calculation results obtained by multiobjective optimization parameters conform to the general law in the distribution law of settlement and can achieve a good approximation of the numerical values between local monitoring points and values. However, when SAA data are missing, the parameter inversion results are bad, indicating the importance of SAA monitoring data.

The results show that the multiobjective parameter inversion method can well realize the global approximation and local optimization in the multiobjective parameter inversion of a 300 m high rockfill dam. The results also show that the optimization parameters can well reflect the deformation characteristics of rockfill materials under actual engineering conditions and that the method is accurate and reliable.

6. Conclusions

This study was the first to utilize SAA in a 300 m ultrahigh rockfill dam, which significantly enhanced the monitoring capabilities of the dam while minimizing construction-related interference and difficulties. SAAs can be vertically buried in the inclinometer pipe for long-term monitoring and easily replaced. With numerous monitoring points,

SAAs provide more comprehensive internal deformation monitoring than other instruments. This ultrahigh rockfill dam has 1147 effective monitoring points, enriching the monitoring data and enabling the use of multisource data for parameter inversion.

Using new settlement monitoring data from the SAA instrument, we proposed a multiobjective parameter inversion method that adapts to the multimaterial zoning and multisource monitoring layout of the 300 m rockfill dam. We used the NSGA-III algorithm to optimize and coordinate the inversion process and fully utilized the multisource monitoring data of each subarea to enhance the accuracy of parameter inversion. We optimize the overall parameters of the rockfill dam and coordinate with the multimaterial zones, so that the parameters of each material zone can be optimized at the same time. Furthermore, through parameter inversion, we have validated the significance of SAA data, demonstrating that SAA can contribute to both deformation monitoring and prediction of dam body simultaneously.

To improve the accuracy of monitoring data in the future, we will strive to investigate ways to properly process SAA data when they fluctuate significantly. To provide a more thorough result, we will simultaneously enrich the parameter inversion process and update and refine the surrogate model and optimization method utilized in parameter inversion.

Data Availability

The data that support the findings of this study are available from the corresponding author upon reasonable request.

Conflicts of Interest

The authors declare that they have no conflicts of interest.

Authors' Contributions

Zhitao Ai worked on methodology, software, investigation, writing-original draft, writing-review and editing. Gang Ma worked on conceptualization, methodology, software, investigation, writing-review and editing, supervision, and funding acquisition. Guike Zhang worked on software, methodology, and investigation. Xiang Cheng worked on software. Quancheng Zou worked on software and investigation. Wei Zhou worked on funding acquisition.

Acknowledgments

The authors would like to thank Professor Ma Gang for his diligent guidance as the mentor. This research was funded by the National Key Research and Development Program of China (Grant no. 2022YFC3005505), National Natural Science Foundation of China (Grant no. 52179141), the Fundamental Research Funds for the Central Universities (Grant no. 2042023kfyq03), Key Program of Science and Technology of Yunnan Province (Grant nos. 202202AF080004 and 202203AA080009), and Study on Life Cycle Deformation Prediction of Ultrahigh Core Rockfill Dam of Yalong Lianghekou Hydropower Station (Grant no. YLLHK-LHA-2020003).

References

[1] H. Q. Ma, "300 m grade concrete faced rockfill dam adaptability and countermeasures," *China Engineering Science.*, vol. 13, no. 12, pp. 4–8.

[2] H. Ma and F. Chi, "Major technologies for safe construction of high earth-rockfill dams," *Engineering*, vol. 2, no. 4, pp. 498–509, 2016.

[3] W. Zhou, G. Ma, J. Liu, X. Chang, S. Li, and K. Xu, "Review of macro- and mesoscopic analysis on rockfill materials in high dams," *Scientia Sinica Technologica*, vol. 48, no. 10, pp. 1068–1080, 2018.

[4] S. Siyuan, M. Nengwu, G. Peiqing, H. Jiandong, and L. Jiaren, "Discussion on innovation technology of safety monitoring engineering for super-high core rockfill dam," *Yangtze River*, vol. 41, pp. 5–8, 2010.

[5] L. Zhizhong, L. Jie, Z. Shuihua, and W. Xi, "Some improvement measures of water level settlement gauge," *Hydropower Automation and Dam Monitoring*, vol. 34, pp. 31–33, 2010.

[6] G. Yongming, C. Shulian, and W. Wei, "Technical summary of monitoring method for CFRD body settlement," *Northwest Hydropower*, vol. 1, pp. 67–70, 2011.

[7] S. M. Majhi, A. Mirzaei, H. W. Kim, S. S. Kim, and T. W. Kim, "Recent advances in energy-saving chemiresistive gas sensors: a review," *Nano Energy*, vol. 79, Article ID 105369, 2021.

[8] Y. Wu, J. Kuang, and X. Niu, "Wheel-INS2: multiple MEMS IMU-based dead reckoning system with different configurations for wheeled robots," *IEEE Transactions on Intelligent Transportation Systems*, vol. 24, no. 3, pp. 3064–3077, 2023.

[9] X. Liu, A. J. Whalen, S. W. Lee et al., "MEMS micro-coils for magnetic neurostimulation," *Biosensors and Bioelectronics*, vol. 227, Article ID 115143, 2023.

[10] H. F. Liu, Z. Luo, Z. Hu et al., "A review of high-performance MEMS sensors for resource exploration and geophysical applications," *Petroleum Science*, vol. 19, no. 6, pp. 2631–2648, 2022.

[11] V. Bennett, T. Abdoun, L. Danisch, T. Shantz, and D. Jang, "Unstable slope monitoring with a wireless shape-acceleration array system," in *Proceedings of the Sventh International Symposium on Field Measurements in Geomechanics*, Boston, Massachusetts, September 2007.

[12] D. D. Dasenbrock, T. Abdoun, and V. Bennett, "Real-time structural health monitoring of landslides and geotechnical assets with shapeaccelarrays," in *Geo-Frontiers 2011*, American Society of Civil Engineers Reston, VI, USA, 2011.

[13] Z. Wang, Y. Jia, X. Liu et al., "In situ observation of storm-wave-induced seabed deformation with a submarine landslide monitoring system," *Bulletin of Engineering Geology and the Environment*, vol. 77, no. 3, pp. 1091–1102, 2017.

[14] R. Yan, W. A. Take, N. A. Hoult, J. Meehan, and C. Levesque, "Evaluation of shape array sensors to quantify the spatial distribution and seasonal rate of track settlement," *Transportation Geotechnics*, vol. 27, Article ID 100487, 2021.

[15] Q. Ren, M. Li, H. Li, L. Song, W. Si, and H. Liu, "A robust prediction model for displacement of concrete dams subjected to irregular water-level fluctuations," *Computer-Aided Civil and Infrastructure Engineering*, vol. 36, no. 5, pp. 577–601, 2021.

[16] K. T. T. Bui, J. F. Torres, D. Gutiérrez-Avilés, V. H. Nhu, D. T. Bui, and F. Martínez-Álvarez, "Deformation forecasting

of a hydropower dam by hybridizing a long short-term memory deep learning network with the coronavirus optimization algorithm," *Computer-Aided Civil and Infrastructure Engineering*, vol. 37, no. 11, pp. 1368–1386, 2022.

[17] K. Yao, Z. Wen, L. Yang, J. Chen, H. Hou, and H. Su, "A multipoint prediction model for nonlinear displacement of concrete dam," *Computer-Aided Civil and Infrastructure Engineering*, vol. 37, no. 14, pp. 1932–1952, 2022.

[18] S. Guan, T. Qu, Y. T. Feng, G. Ma, and W. Zhou, "A machine learning-based multi-scale computational framework for granular materials," *Acta Geotechnica*, vol. 18, no. 4, pp. 1699–1720, 2022.

[19] S. Li, Z. Yang, X. Tian, Y. Xiao, X. Li, and X. Liu, "Influencing factors of scale effects in large-scale direct shear tests of soil-rock mixtures based on particle breakage," *Transportation Geotechnics*, vol. 31, Article ID 100677, 2021.

[20] H. Yu, X. Wang, B. Ren, T. Zeng, M. Lv, and C. Wang, "An efficient Bayesian inversion method for seepage parameters using a data-driven error model and an ensemble of surrogates considering the interactions between prediction performance indicators," *Journal of Hydrology*, vol. 604, Article ID 127235, 2022.

[21] J. Li, C. Chen, Z. Wu, and J. Chen, "Multi-source data-driven unsaturated seepage parameter inversion: application to a high core rockfill dam," *Journal of Hydrology*, vol. 617, Article ID 129171, 2023.

[22] Y. Xu and Z. Wu, "Parameter identification of unsaturated seepage model of core rockfill dams using principal component analysis and multi-objective optimization," *Structures*, vol. 45, pp. 145–162, 2022.

[23] W. Li and Z. Wu, "A methodology for dam parameter identification combining machine learning, multi-objective optimization and multiple decision criteria," *Applied Soft Computing*, vol. 128, Article ID 109476, 2022.

[24] Y. Li, M. A. Hariri-Ardebili, T. F. Deng, Q. Wei, and M. Cao, "A surrogate-assisted stochastic optimization inversion algorithm: parameter identification of dams," *Advanced Engineering Informatics*, vol. 55, Article ID 101853, 2023.

[25] C. Guo, G. Ma, H. Xiao et al., "Displacement back analysis of reservoir landslide based on multi-source monitoring data: a case study of the cheyiping landslide in the lancang river basin, China," *Remote Sensing*, vol. 14, no. 11, p. 2683, 2022.

[26] W. Zhou, S. L. Li, G. Ma, X. L. Chang, X. Ma, and C. Zhang, "Parameters inversion of high central core rockfill dams based on a novel genetic algorithm," *Science China Technological Sciences*, vol. 59, no. 5, pp. 783–794, 2016.

[27] F. Kang, Y. Wu, J. Li, and H. Li, "Dynamic parameter inverse analysis of concrete dams based on Jaya algorithm with Gaussian processes surrogate model," *Advanced Engineering Informatics*, vol. 49, Article ID 101348, 2021.

[28] J. Wan, *Design and Implementation of High Precision MEMS Micro Inertial Attitude System*, The Institute for Global Environmental Strategies, Hayama, Kanagawa, 2019.

[29] Z. Liu, X. Wang, and W. Ni, "Research on attitude angle measurement with high precision based on MEMS sensors," *China Measurement and Test*, vol. 43, no. 2, pp. 6–12, 2017.

[30] Z. Chen, Y. Yin, J. Yu, X. Cheng, D. Zhang, and Q. Li, "Internal deformation monitoring for earth-rockfill dam via high-precision flexible pipeline measurements," *Automation in Construction*, vol. 136, Article ID 104177, 2022.

[31] G. Hou, Z. Li, Z. Hu, D. Feng, H. Zhou, and C. Cheng, "Method for tunnel cross-section deformation monitoring based on distributed fiber optic sensing and neural network," *Optical Fiber Technology*, vol. 67, Article ID 102704, 2021.

[32] J. R. Gage, D. Fratta, A. L. Turner, M. M. MacLaughlin, and H. F. Wang, "Validation and implementation of a new method for monitoring in situ strain and temperature in rock masses using fiber-optically instrumented rock strain and temperature strips," *International Journal of Rock Mechanics and Mining Sciences*, vol. 61, pp. 244–255, 2013.

[33] Z. L. Zhang, J. Yan-An, and B. Y. Zhang, "Comparison and verification of constitutive models for rockfill materials under complex stress path," *Rock and Soil Mechanics*, vol. 29, no. 5, 2008.

[34] W. Dong, L. Hu, Y. Z. Yu, and H. Lv, "Comparison between duncan and Chang's EB model and the generalized plasticity model in the analysis of a high earth-rockfill dam," *Journal of Applied Mathematics*, vol. 2013, Article ID 709430, 12 pages, 2013.

[35] K. Deb, A. Pratap, S. Agarwal, and T. Meyarivan, "A fast and elitist multiobjective genetic algorithm: NSGA-II," *IEEE Transactions on Evolutionary Computation*, vol. 6, no. 2, pp. 182–197, 2002.

[36] J. Zhan, Y. Li, Y. Liu, H. Li, S. Zhang, and L. Lin, "NSGA-II-Based Granularity-Adaptive Control-Flow Attestation," *Security and Communication Networks*, vol. 56, no. 3, 2021.

[37] Y. Liu, K. You, Y. Jiang et al., "Multi-objective optimal scheduling of automated construction equipment using non-dominated sorting genetic algorithm (NSGA-III)," *Automation in Construction*, vol. 143, Article ID 104587, 2022.

[38] F. R. Adaryani, S. Jamshid Mousavi, and F. Jafari, "Short-term rainfall forecasting using machine learning-based approaches of PSO-SVR, LSTM and CNN," *Journal of Hydrology*, vol. 614, Article ID 128463, 2022.

[39] D. Zhang, G. Ma, Z. Deng, Q. Wang, G. Zhang, and W. Zhou, "A self-adaptive gradient-based particle swarm optimization algorithm with dynamic population topology," *Applied Soft Computing*, vol. 130, Article ID 109660, 2022.

[40] R. A. Zitar, M. A. Al-Betar, M. A. Awadallah, I. A. Doush, and K. Assaleh, "An intensive and comprehensive overview of JAYA algorithm, its versions and applications," *Archives of Computational Methods in Engineering*, vol. 29, no. 2, pp. 763–792, 2022.

[41] N. Fahem, I. Belaidi, A. Oulad Brahim, M. Noori, S. Khatir, and M. Abdel Wahab, "Prediction of resisting force and tensile load reduction in GFRP composite materials using Artificial Neural Network-Enhanced Jaya Algorithm," *Composite Structures*, vol. 304, Article ID 116326, 2023.

[42] S. Sharma and V. Kumar, "A comprehensive review on multi-objective optimization techniques: past, present and future," *Archives of Computational Methods in Engineering*, vol. 29, no. 7, pp. 5605–5633, 2022.

[43] N. Gunantara, "A review of multi-objective optimization: methods and its applications," *Cogent Engineering*, vol. 5, no. 1, pp. 1502242–1502316, 2018.

[44] Y. Cui, Z. Geng, Q. Zhu, and Y. Han, "Review: multi-objective optimization methods and application in energy saving," *Energy*, vol. 125, pp. 681–704, 2017.

[45] K. Deb and H. Jain, "An evolutionary many-objective optimization algorithm using reference-point-based non-dominated sorting approach, part I: solving problems with box constraints," *IEEE Transactions on Evolutionary Computation*, vol. 18, no. 4, pp. 577–601, 2014.

[46] H. Jain and K. Deb, "An evolutionary many-objective optimization algorithm using reference-point based non-dominated sorting approach, part II: handling constraints and extending to an adaptive approach," *IEEE Transactions on Evolutionary Computation*, vol. 18, no. 4, pp. 602–622, 2014.